This is a repository copy of *Study of phase separation in an InGaN alloy by electron energy loss spectroscopy in an aberration corrected monochromated scanning transmission electron microscope*.

White Rose Research Online URL for this paper:
http://eprints.whiterose.ac.uk/110006/

Version: Accepted Version

Article:

Walther, T. orcid.org/0000-0003-3571-6263, Wang, X., Angadi, V.C. orcid.org/0000-0002-0538-4483 et al. (3 more authors) (2016) Study of phase separation in an InGaN alloy by electron energy loss spectroscopy in an aberration corrected monochromated scanning transmission electron microscope. Journal of Materials Research. ISSN 0884-2914

https://doi.org/10.1557/jmr.2016.447

This article has been published in a revised form in Journal of Materials Research [https://doi.org/10.1557/jmr.2016.447]. This version is free to view and download for private research and study only. Not for re-distribution, re-sale or use in derivative works. © Materials Research Society 2016.

Reuse

This article is distributed under the terms of the Creative Commons Attribution-NonCommercial-NoDerivs (CC BY-NC-ND) licence. This licence only allows you to download this work and share it with others as long as you credit the authors, but you can’t change the article in any way or use it commercially. More information and the full terms of the licence here: https://creativecommons.org/licenses/

Takedown

If you consider content in White Rose Research Online to be in breach of UK law, please notify us by emailing eprints@whiterose.ac.uk including the URL of the record and the reason for the withdrawal request.

eprints@whiterose.ac.uk
https://eprints.whiterose.ac.uk/

DOI: https://doi.org/10.1557/jmr.2016.447

Study of phase separation in an InGaN alloy by electron energy loss spectroscopy in an aberration corrected monochromated scanning transmission electron microscope

Thomas Walther[1*], Xiaoyi Wang[1], Veerendra C Angadi[1], Pierre Ruterana[2], Paolo Longo[3] and Toshihiro Aoki[4]

[1] Dept. Electronic & Electrical Eng., Kroto Centre for High-Resolution Imaging and Spectroscopy, University of Sheffield, North Campus, Wheeldon Street, Sheffield S3 7HQ, UK
[2] CIMAP, UMR 6252, CNRS-ENSICAEN-CEA-UCBN, 14050 Caen, cedex, France
[3] Gatan, 780 Commonwealth Drive, Warrendale, PA 15086, USA
[4] LeRoy Eyring Center for Solid State Science, Arizona State University, Tempe, AZ 85287, USA

[*]Email of corresponding author: t.walther@sheffield.ac.uk

ABSTRACT

Phase separation of $In_xGa_{1-x}N$ into Ga-rich and In-rich regions has been studied by electron energy-loss spectroscopy (EELS) in a monochromated, aberration corrected scanning transmission electron microscope (STEM). We analyse the full spectral information contained in EELS of InGaN, combining for the first time studies of high-energy and low-energy ionization edges, plasmon and valence losses. Elemental maps of the N K, In $M_{4,5}$ and Ga $L_{2,3}$ edges recorded by spectrum imaging at 100kV reveal sub-nm fluctuations of the local indium content. The low energetic edges of Ga $M_{4,5}$ and In $N_{4,5}$ partially overlap with the plasmon peaks. Both have been fitted iteratively to a linear superimposition of reference spectra for GaN, InN and InGaN, providing a direct measurement of phase separation at the nm-scale. Bandgap measurements are limited in real space by scattering delocalization rather than the electron beam size to ~10nm for small bandgaps, and their energetic accuracy by the method of fitting the onset of the joint density of states rather than energy resolution. For an $In_{0.62}Ga_{0.38}N$ thin film we show that phase separation occurs on several length scales.

I. INTRODUCTION

Optoelectronic devices based on ternary InGaN alloys can cover a wide range of optical emission and absorption wavelengths, from near ultraviolet (GaN) to infrared (InN). However, InGaN growth is complex and a number of phenomena such as ordering [1] crystallographic defects [2] as well as phase separation [3-6] may significantly influence the performance of light emitting devices (LEDs). Phase separation of $In_xGa_{1-x}N$ alloys into Ga-rich and In-rich regions was first predicted by Ho and Stringfellow [7] and later observed by a number of research groups, particularly for InGaN samples of medium high In content grown at high temperatures. As the indium concentration controls the optical properties of InGaN, both wavelength and efficiency of optical emission, it is important to quantify any degree of phase separation in an InGaN thin film. Matsuoka et al. [8] reported the growth of InGaN alloys by low temperature (500^{o}C) metalorganic chemical vapour deposition (MOCVD) with In concentration up to 42%, while other studies [9-12] indicated that growth of InGaN thin films and $In_xGa_{1-x}N/In_yGa_{1-y}N$ heterostructures by MOCVD at temperatures between700^{o}C and 800^{o}C may maximally achieve x=30%.

Previously, a reliable quantification of the degree of phase separation was only possible by Rutherford backscattering spectrometry (RBS). Due to the radiation sensitivity of InGaN to beam damage by 200keV electrons, as observed by O'Neill et al. [13] and later Smeeton et al. [14], high electron fluxes as typically used in extended high-resolution imaging in transmission electron microscopy (TEM) or core-loss electron energy-loss spectroscopy (EELS) may lead to erroneous results. Humphreys discussed the controversy about TEM evidence for indium clustering in InGaN in great detail [15]. A more recent STEM study suggested a knock-on threshold of >120keV for atomic displacement in InGaN [16] and our EELS experiments were all conducted below that energy, at 100 and 60kV.

Also, low-loss EELS can yield spectra of the plasmon loss regions at much lower electron fluxes and so potentially circumvent beam damage in the TEM. Unfortunately, the low energetic core loss signals of gallium (Ga 3d transitions yield $M_{4,5}$ peaks at 23.8 and 28.5eV) and indium (In 4d transitions yield $N_{4,5}$ peaks at 20.0 and 25.9eV) directly overlap with the plasmon peaks, which shift from 19.35eV for GaN to 15.5eV for InN.

We have recently found first evidence for phase separation in several $In_xGa_{1-x}N$ thin films with x>0.5 by fitting both plasmon and low-energy core losses over the energy range of 13-30eV in single electron energy-loss spectra acquired at 197keV at low electron beam density [17] and now extend this method to multiple linear-least squares (MLLS) regression to complete InGaN EELS spectrum images, including monochromated valence electron energy loss spectra (VEELS). We also assess the bandgap of the alloys using different fitting routines for the region of valence electron excitation, demonstrating both the possibility to measure bandgaps down to <2eV with a monochromator and the significance of scattering delocalization at such low energies, which means a spatial resolution of ~10nm is achieved despite a much smaller electron beam size. As a typical example for an alloy with x>0.5 from the above series of samples, all of which showed some degree of facetted island growth and strong speckles in weak-beam dark-field imaging [18], we have chosen an $In_{0.62}Ga_{0.38}N$ thin film for this exemplary study.

II. EXPERIMENTAL

A. Growth of InGaN sample

The investigated InGaN sample was grown on c-plane sapphire by metal organic vapour phase epitaxy (MOVPE) in a close couple shower head AIXTRON reactor using triethyl-gallium (TEGa) and trimethyl-indium (TMIn) for the metals and NH_3 for nitrogen. The growth temperature was 550°C, the growth chamber pressure was 200 mbar and the group- V/III ratio 110000, yielding a nominal indium content of x=0.62. An electron transparent cross-sectional sample was prepared using standard mechanical pre-treatments (glueing, cutting, grinding, dimple polishing) followed by argon ion milling in a Gatan PIPS at 5 keV initially, with final polishing at 0.6 keV. Care was taken to avoid conditions which would thin the sample quickly but could introduce ion beam damage: the sample was cooled by liquid nitrogen during the ion milling process, and the angle of ion incidence was kept at nominally 5°. The resulting surface amorphous layers observed in the transmission electron microscope were only a few nm wide.

B. EELS characterization

The electron microscopy experiments were carried out using two different instruments: a JEOL 2010F analytical TEM equipped with a Schottky field-emission gun was used for investigation of thicker specimen regions with 9.5mrad convergence semi-angle at 197kV (this voltage allows the user to increase the high tension by up to 3kV for energy-filtered imaging, cf. [19]). A Gatan Imaging Filter (GIF 200) provides an energy resolution of ~0.9 eV (FWHM of zero loss peak). A Nion UltraSTEM 100 with Gatan Enfinium ER energy-loss spectrometer, aberration corrector and monochromator [20] was used with 30mrad convergence semi-angle at 100kV (not monochromated for high core losses, with 0.5eV/channel dispersion) or 60kV (monochromated for low losses, with 0.015eV/channel dispersion). The collection semi-angle was >90mrad for high-angle ADF imaging, 30mrad with 2mm entrance aperture for EELS (used at 60kV)and 45mrad with 3mm entrance aperture for EELS (used at 100kV). The energy resolution was better than 0.35eV without and ~0.15eV with monochromator (FWHM values, including the point spread function of the detector). A ~0.12nm probe size with ~300pA beam current (20-30pA after monochromation) was set up and spectra were acquired with the charge-coupled device (CCD) detector in single read-out vertical integration mode and binning for fast acquisition to avoid electron beam-induced damage of the sample. Only the combination of monochromator with aberration corrector enabled the formation of a small electron beam of sufficient current suitable for high-quality VEELS for both bandgap extraction and plasmon fitting.

III. RESULTS AND DISCUSSION

The investigated sample is one from a series of $In_xGa_{1-x}N$ thin films of different indium content. The initially flat film surfaces have been shown to roughen with increasing value of x, leading to islands with pronounced facets for $x>0.5$. At the same time, dark field imaging has shown a corresponding increase in speckle contrast from the alloys [18]. This is exactly the compositional range for which phase separation has previously been identified as likely from X-ray diffraction [21]. While such high indium content is not typical for present InGaN quantum wells used for commercial LEDs, it may become relevant in the future if lower bandgaps will be approached to circumvent the use of yellow phosphors in combination with blue LEDs to produce green, or orange, light emission more directly [22]. Moreover, carrier confinement in thin quantum wells and small quantum dots can complicate the interpretation of emission and bandgap properties, so our thin film sample can serve as an easier to understand model system. A typical overview image of our sample with $x_{nom}=0.62$ is depicted in figure 1 where several facetted islands can be clearly seen. Some of these seem to preferentially nucleate above apparent holes in the underlying film, however, these holes are partially filled by carbonaceous species and it is not yet clear whether they are an artefact from preferential argon ion thinning and subsequent filling by sputtered glue. We have used integral measurements by energy-dispersive X-ray spectroscopy (EDXS) at 197kV to verify the average In content of each sample, using a recently improved quantification method based on thickness-dependent, self-consistent k-factors [23,24] which eliminates discrepancies between absorption corrections for areas of different thicknesses [25] and has given excellent linearity with the observed shift of the plasmon peak energy in EELS [18]. None of the regions investigated at higher magnifications in subsequent figures can be marked in the overview of figure 1 because, being much thinner, they are outside its field of view, as we tried to avoid irradiating these regions at 200kV prior to chemical analysis at 60-100kV, which could have implied beam electron beam damage as explained above.

FIG. 1. ADF STEM image of cross-sectioned $In_{0.62}Ga_{0.38}N$ thin film at low magnification. JEOL 2010F, 197kV, 9.5mrad convergence semi-angle, 55-170mrad collection angle, 2.5 μm field of view.

In figure 2 we show results from an investigation of a very small area at high magnification by mapping high-energy core losses in EELS at 100kV without monochromation.

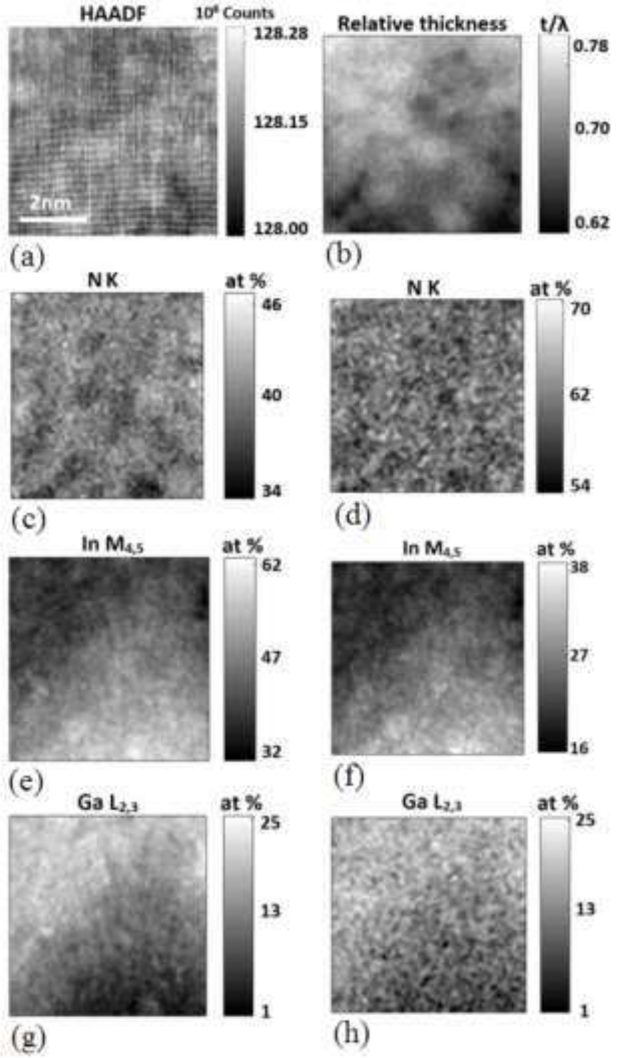

FIG. 2. (a) HA-ADF-STEM image of cross-sectioned $In_{0.62}Ga_{0.38}N$ film at high magnification, about 10nm above the GaN substrate, showing (0002) lattice fringes. Growth direction points upwards. (b) Relative thickness map (t/λ) in multiples of the inelastic mean free path, λ. (c-h) Results from spectrum imaging: elemental maps of (c,d) nitrogen from N K edge, (e,f) indium from In M4,5 edge, (g,h) gallium from Ga L2,3 edge, recorded at 100kV and calculated using (c,e) integration after inverse power law subtraction, (g) integration after exponential background extrapolation or (d,f,g) from model based multiple linear-least squares fitting of the edge intensities, all normalized to a sum of unity for all three elements. NION UltraSTEM, 100kV, 30mrad convergence semi-angle, 90 mrad inner collection angle (HA-ADF), 45 mrad collection angle (EELS), 50ms dwell time per pixel, 128 x 128 pixel, 0.5eV/channel, 7nm field of view.

Figure 2(a) displays a high-angle annular dark-field (HA-ADF) image of a section ~7nm wide near the bottom of the InGaN thin film, close to a <1-100> zone axis orientation. The growth direction points upwards, and clear (0002) lattice fringes (d_{0002}=0.26nm) running along the horizontal and in some areas weak (11-20) lattice fringes ($d_{11\text{-}20}$=0.16nm) along the vertical are visible. The apparent waviness of the lattice planes is due to slight thermal drift using the acquisition. We did not use any drift correction as this would have necessitated additional reference image collection and thus would have slowed down acquisition and increased the total dose. All images and maps shown were acquired rotated through almost 90°, and the fine vertical stripes visible in parts of figure 2(a) are due to emission fluctuations typical of the cold field emitter. Figure 2(b) is a relative thickness map of the area calculated from the intensity ratio of the zero loss peak to the total intensity, and when we use a value of λ=55±9nm for the inelastic mean free path extrapolated from tabulated semiconductor values recorded at 100kV for different acquisition angles (Table 5.2 on page 304 of [26]) the value of t/λ=0.69±0.03 measured for this sample region would indicate the specimen area investigated here is slightly less than 40nm thin. The above inelastic mean free path is smaller than typical values for most semiconductors at 100 or 200kV because of the large entrance aperture used (45mrad reduces λ to ¾ of the value for 10mrad listed in [26]), and the heavy indium atoms in $In_{0.6}G_{0.4}N$ reduce it even further. Figures 2(c-h) are elemental maps of the distribution of the three elements nitrogen, indium and gallium calculated using two different methods for fitting the data, using either a pixel-wise automated edge detection routine [27] with inverse power-law or exponential background fit and subtraction in the pre-edge regions, net integration over certain ranges and quantification using tabulated Hartree-Slater cross-sections or a recursive multiple linear-least squares fitting to Hartree-Slater models of edges tabulated in Gatan Digital Micrograph GMS3 software [28]. The speckle contrast in these maps is a superposition of shot noise (which should depend only on the acquired data and therefore be the same in left and right columns) but also to some degree due to the different background subtraction and fit procedures (where the two algorithms used differ). The relative quantification has been normalised to a sum of unity taking into account only these three elements. There was a very faint oxygen signal from the surface which has been neglected. Both methods agree, within noise levels, for the quantification of the gallium content from the Ga L edge (g: 15.2±5.9 at%, h: 14.6±4.5 at%), which would imply an average x value for $In_xGa_{1-x}N$ of x=0.7±0.1. The Ga L-edge starts at very high energy (1115eV) so its intensity is weak and the maps will be mainly limited by shot noise, while background subtraction is relative straight forward and implies small systematic errors. For the quantification of the N K-edge and the In M-edge the situation is reversed: these edges lie at lower energies and so have plenty of intensity but they partially overlap (the N K-edge starts at 400eV, the In M-edge at 443eV) so they are more difficult to separate. Correspondingly, the indium maps in (e) and (f) show the same features but on different contrast levels (e: 48.9±5.4 at% indium; f: 25.5±4.2 at% indium). The quantification with the higher apparent indium signal predicts less nitrogen, and vice versa. The nitrogen content as calculated from the N K-edge by the two algorithms lies either below the stoichiometric 50at% value (c: 35.9±1.5 at%) or above (d: 60.9±2.1 at%), indicating systematic errors of about the same magnitude but in opposite directions where our algorithm [27] systematically underestimates the N content by about as much as the commercial algorithm [28] overestimates it. Deconvolution of the spectra could change the relative quantification further but has not yet been attempted here, as it would have been difficult to record low- and high-loss spectra without the dual-EELS option [29] and we could use integration ranges sufficiently wide for the N and Ga edges to include plasmon replicas so (multiple) plasmon scattering would cancel out in the ratio approach taken. However, it should be stated that the relative quantification of InGaN is a real challenge, firstly, as it implies evaluating three ionization edges of different types (K, L and M) and, secondly, because two edges of these overlap significantly. The standard deviations of the N maps in (c) and (d) are very small, as would be expected for a constant group-V sub-lattice consisting of N only. The maps for In and Ga show much larger scatter, with 2-3 times higher standard deviations. The lateral scale of the indium-rich regions visible in (e) and (f) extends to only 0.5-3nm, which would be in agreement with [30] . Given the projection through the ~40nm thick specimen such In-rich clusters, should they exist and not be an artefact from electron irradiation, must consist of almost pure InN. Extremely short-range fluctuations of the chemical composition (on a lateral scale <1nm) have been speculated about previously while medium range order on the scale >2nm was shown to not influence the optical properties of InGaN quantum wells [31], which agrees with our findings shown later in figure 10.

TABLE I: processing details for elemental maps displayed in figure 2

element	edge type	background subtraction method for left column	integration range [eV] for left column	fit method for maps in right column
In	M	inverse power-law	247	Hartree-Fock model in Gatan's Digital Micrograph GMS3
Ga	L	exponential	189	
N	K	inverse power-law	51	

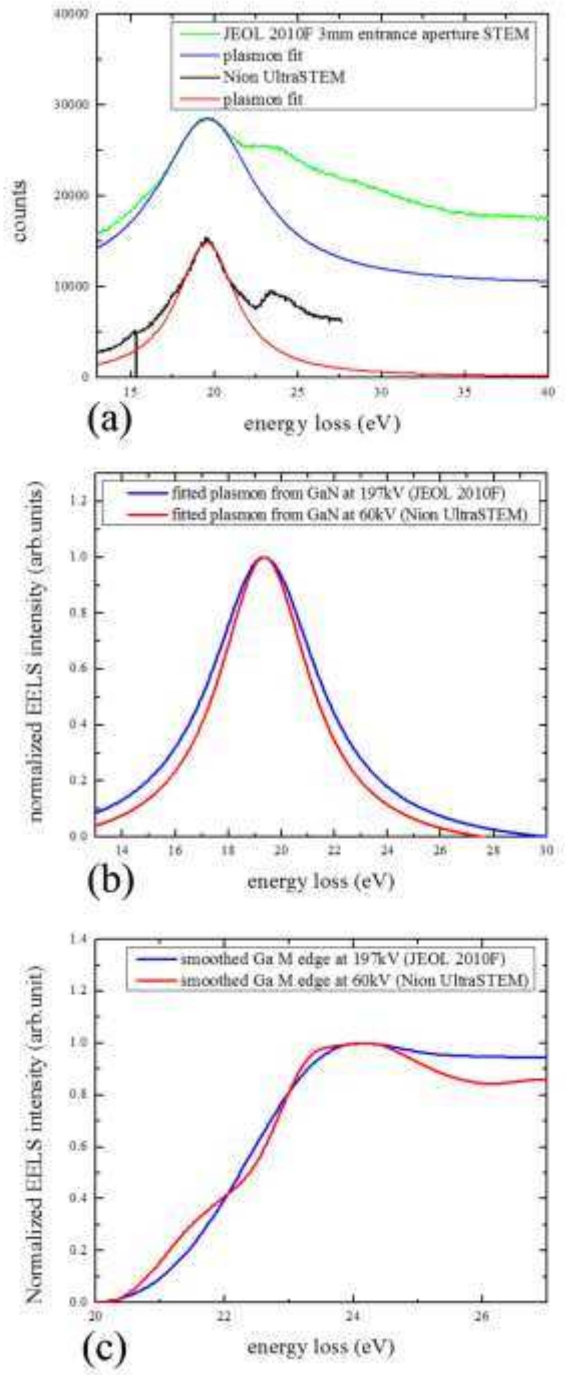

FIG. 3. Comparison of (a) low-loss EELS from GaN recorded at 197 kV in the JEOL 2010F (green, with blue fit to plasmon) and at 60kV in the NION UltraSTEM (black, with red fit to plasmon). Comparison of fits for (b) plasmon loss and (c) Ga M-edge core loss components.

In order to suppress the beam damage issue already mentioned we have also performed EELS at a reduced acceleration voltage of 60kV where potential knock-on damage should be completely negligible, even at higher dose. A comparison of monochromatic EELS at 60kV in the Nion UltraSTEM with cold field-emitter to EELS at 197kV in a standard JEOL 2010F with Schottky-field emitter has been performed for pure GaN. Figure 3 shows (a) raw spectra with Lorentz fits of the plasmons for both microscopes (from 13-40 eV for the 197keV spectrum and 13-27eV for the 60kV spectrum), and best fits for (b) the plasmon loss component and (c) the Ga M core loss component only where the latter was extracted as the remainder after fitting the plasmon peak by a Lorentz function as shown and then subtracting it off from a smoothed version of the low-loss spectrum. The zero loss peak was subtracted prior to the fits and thus not included. The differences are subtle, with a slightly reduced plasmon peak width and a slight undulation of the Ga core loss signal at the lower acceleration voltage which we tentatively attribute to the individual onsets of M_5, M_4 and M_3 partial edges that become visible when the acceleration voltage is reduced, the energy resolution improved and the collection angle increased. In other words, the plasmon has not really become narrower at lower acceleration voltage but the fitting routine transferred some of the broadening of the core losses at 197kV due to the higher aberrations of the older spectrometer to the plasmon loss region. This directly meant that the database of InGaN reference spectra previously acquired for 197kV in the JEOL microscope (see figure 4a) had to be compiled afresh, now for monochromated measurements at 60kV. Our approach was to extract high quality spectra from the GaN buffer region and the InGaN layer, and to subtract the Ga core losses from figure 3(c) from the latter to obtain references for pure InN, then interpolating InGaN data in a way analogous to the one described in [17]. This resulted in the new set of compiled InGaN reference spectra shown in figure 4(b).

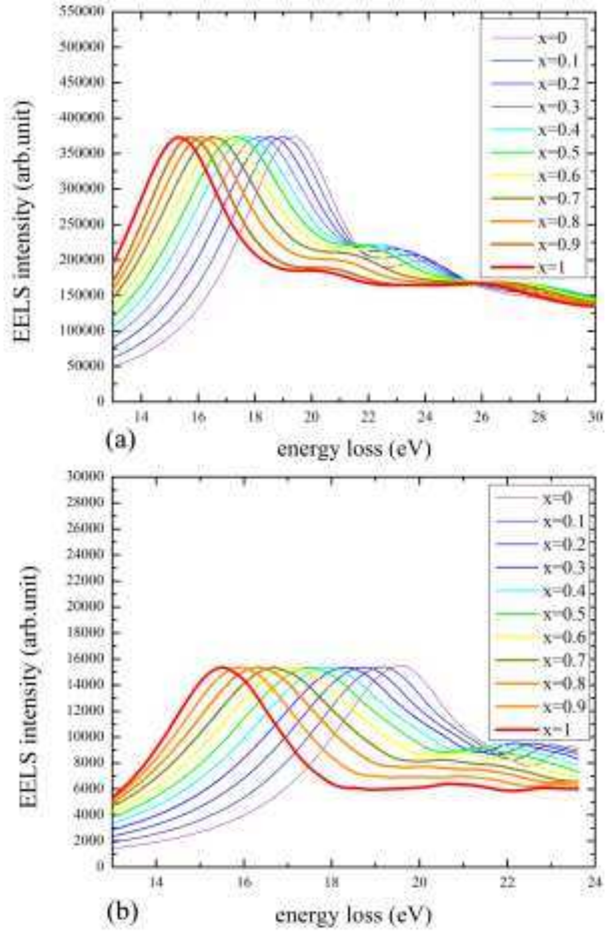

FIG. 4. Comparison of GaN reference spectra for x=0 to x=1 at (a) 197kV [17] and (b) 60kV. Note the different scale chosen to correlate with the experimental dispersions of (a) 0.05eV/channel (1024 channels) and (b) 0.015eV/channel (2048 channels).

Figure 4 compares reference EELS spectra for InGaN alloys of different indium content, x, generated from experimental spectra recorded for GaN, InN and some InGaN alloy thin films whose average x values were previously determined by EDXS. These spectra are used as database for multiple linear least-squares fitting. In this work, we used the data shown in figure 4(b) for monochromated EELS at 60kV.

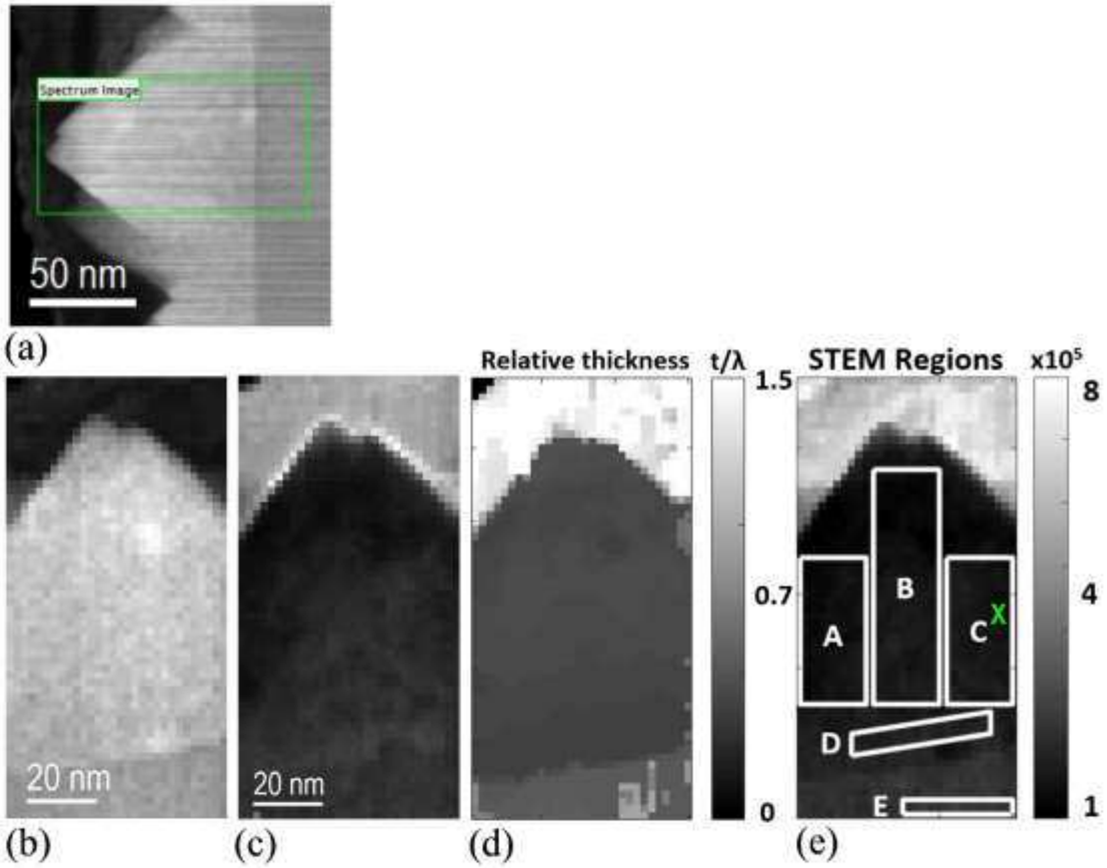

FIG. 5. (a) ADF overview image of InGaN islands, grown from right to left, with scan lines visible due to fast acquisition (32µs dwell time per pixel, 500 x 500 pixel, as acquired), (b) rotated ADF image of the area investigated with 2.1nm sampling where the apparent slight tilt from vertical growth is due to drift during the acquisition of (c) the spectrum image (0.5s dwell time per pixel, 30 x 60 pixel, 0.015eV/channel). (d) relative thickness map for spectrum imaging at 60kV, with mean values of t/λ=1.52±0.14 in the top carbon region, 0.43±0.02 in the InGaN layer (which is, hence, almost uniformly thin) and 0.59±0.13 in the GaN buffer. (e) definition of regions A-D in the InGaN and region E in the GaN buffer used later in Table II. The cross marks the position of the spectrum and its fit shown in figure 6(i). Nion UltraSTEM, 30 mrad convergence, 90 mrad inner collection angle for HA-ADF, 45 mrad collection angle for EELS.

A region of the InGaN layer with a facetted island of almost uniform thickness in projection, as shown in figure 5, has been used for further investigation by EELS of the low-loss region up to 24eV. The speckle contrast in figure 5(b) stems from a superposition of carbon contamination and chemical inhomogeneities in this region both of which are unlikely to be due to beam damage as they are already visible in the fast scan acquired prior to the spectrum imaging, as shown in figure 5(a). Extrapolating the inelastic mean free path of 55nm at 100kV to 61nm at 60kV, the above value of t/λ=0.43±0.02 would imply an absolute specimen thickness around 26nm, with an error of ±4nm, but constant over the field of view to within ±1nm. This shows the area investigated in detail in the following is suitably thin and flat.

TABLE II: numerical results for regions of the maps and spectra analyzed. Values in red are considered unreliable (low R^2) while those in green are considered more reliable (high R^2).

region	top	A	B	C	D	E
material	carbon	InGaN (left)	InGaN (centre)	InGaN (right)	InGaN (bottom)	GaN
t/λ (Fig.5d)	1.52±0.14		0.43±0.02			0.59±0.14
x_{In}						
(Fig. 7a)		0.70±0.03	0.69±0.04	0.70±0.02	0.78±0.02	0.14±0.02
(Fig. 7b)		0.72±0.06	0.75±0.07	0.84±0.05	0.89±0.05	0.017±0.010
E_g [eV]						
(Fig. 8b)						3.26-3.38
(Fig. 9a)		1.72±0.07	1.85±0.09	2.00±0.06	1.74±0.10	3.41±0.07
(Fig. 9b)		2.06±0.13	1.96±0.16	1.79±0.08	1.71±0.13	3.17±0.04
(Fig. 9d)		1.85±0.16	1.81±0.26	1.75±0.18	1.22±0.10	3.31±0.08
R^2						
(Fig. 8b)						0.77-0.89
(Fig. 9c)		0.74±0.08	0.71±0.11	0.71±0.08	0.69±0.05	0.69±0.09
(Fig. 9e)		0.81±0.07	0.68±0.17	0.79±0.11	0.39±0.13	0.76±0.14

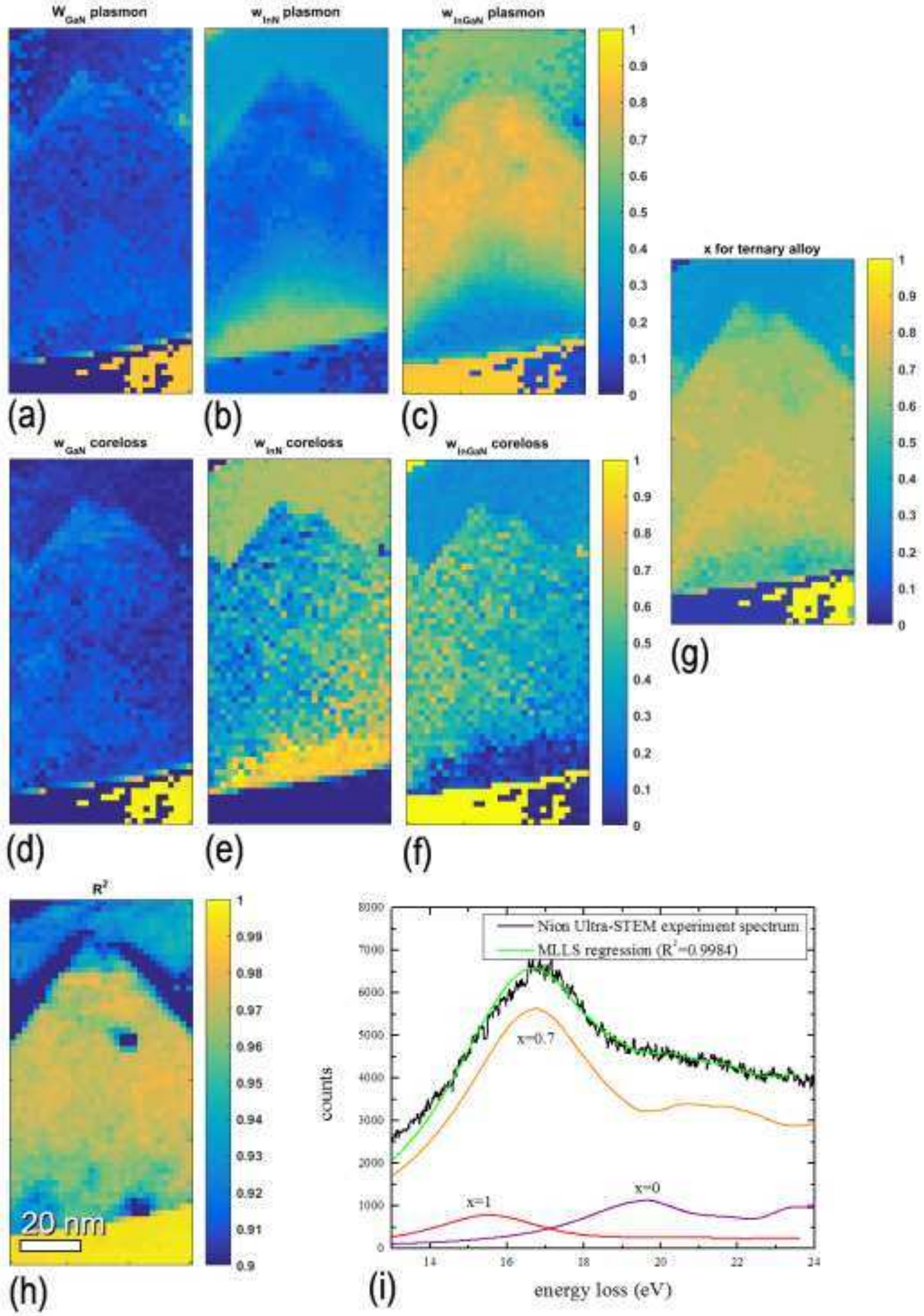

Fig. 6. Results from fitting each spectrum from the spectrum image in figure 5(b) by a linear superposition of three reference spectra, one for GaN, one for InGaN and one for InN film. Shown are the weight parameters attributed to (a,d) GaN, (b,e) InN and (c,f) $In_xGa_{1-x}N$ where x was varied from 0.05 to 0.95 in steps of 0.05. Top row: fit for plasmons, middle row: fit for core losses. (g) plots the best fitting x value of the ternary component only. (h) shows the R^2

parameter of the fit for each spectral data point. (i) shows the fit (green) for the experimental EELS (black) at one particular pixel marked in region C of figure 5(e) based on a weighted superposition of reference spectra from GaN (red), InN (purple) and $In_{0.7}Ga_{0.3}N$ (orange)

Fitting each spectrum within the 2D spectrum image has been performed on a linear least-squares method, decomposing each spectrum into a GaN, an InN and a ternary $In_xGa_{1-x}N$ component where the four fitting parameters are the three relative weight components, w_{GaN}, w_{InN}, w_{InGaN} and the indium component x_{alloy} for the ternary alloy component only. These fit parameters are plotted in figure 6(a-g) for plasmon and core losses. Figure 6(h) shows a plot of the R^2 parameter of the fit, indicating good fit quality, with $R^2>0.9$ in all cases and $R^2>0.98$ in most regions. Two spots within the InGaN with pronounced lower R^2 values probably indicate carbon contamination spots rather than the onset of beam damage, as they are not visible in any of the maps in figure 6(a-g). All weight parameters lie between 0 and 1 without applying any further constraints and are hence physically meaningful. The weights from plasmon and core loss fitting agree extremely well, indicating the lower part of the InGaN is almost pure InN (with some GaN and little $In_{0.5}Ga_{0.5}N$) while the upper part of the island is mostly ternary $In_xGa_{1-x}N$ with x decreasing from x~0.8 to ~0.5 near the surface. The GaN is either fitted as binary GaN (near the bottom right of the maps) or ternary $In_{0.05}Ga_{0.95}N$ (near the bottom left), and this is presumably due to the selection of Δx=0.05 increments for the fitting of the ternary alloy composition (checking for all possible discrete values of the ternary allow component would have slowed down the pointwise fitting procedure enormously).

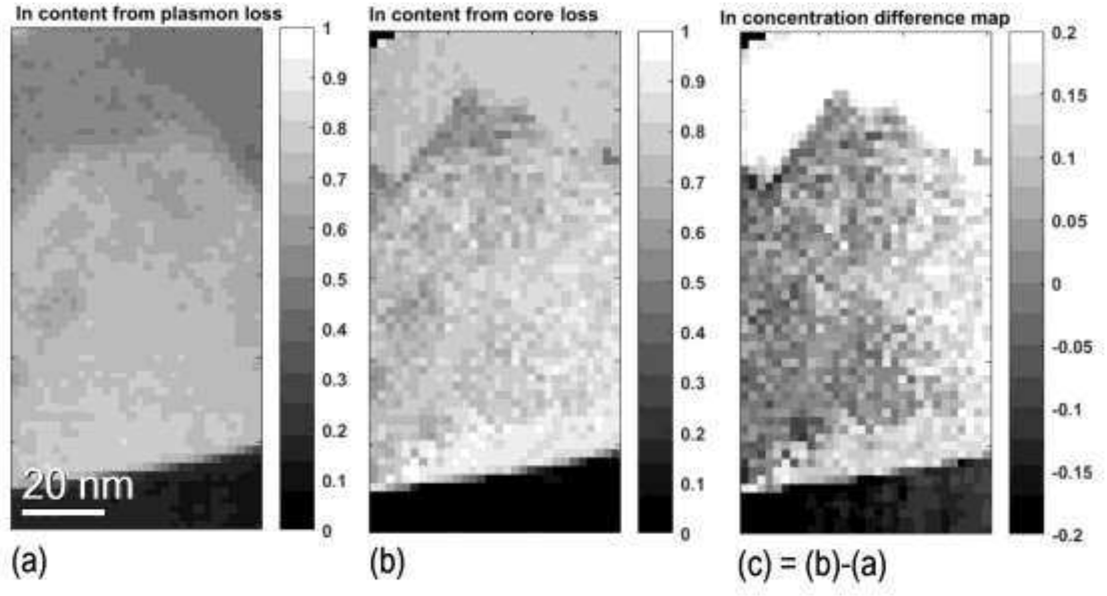

Fig. 7. Maps of indium content, x, calculated for data from figure 6 from weights of fitting (a) plasmon losses, (b) low core-losses, (c) difference map (b)–(a).

Figure 7 compares quantitative maps of the indium content, x, obtained from the relative weights of the plasmon and the low core-loss fits from the previous figure, where $x=w_{InN} + x_{alloy}\, w_{InGaN}$. Generally, the map from the core losses (7b) has somewhat higher contrast but also higher noise levels. The map from the plasmons (7a) appears smoother but lower in overall contrast, and in the GaN the x value predicted lies significantly above zero level. Both methods indicate indium enrichment within the first 15nm of InGaN grown on the GaN buffer, where the core loss fitting would indicate almost pure InN (x~0.9) whereas the plasmon loss fitting would suggest a maximum of around x~0.8. Given the precision of the individual fits, where increments of $\Delta x=0.05$ were tested for the ternary component, error bars of this order may well be expected and the difference between figures 7(a) and 7(b) is typically within this range for most of the InGaN.

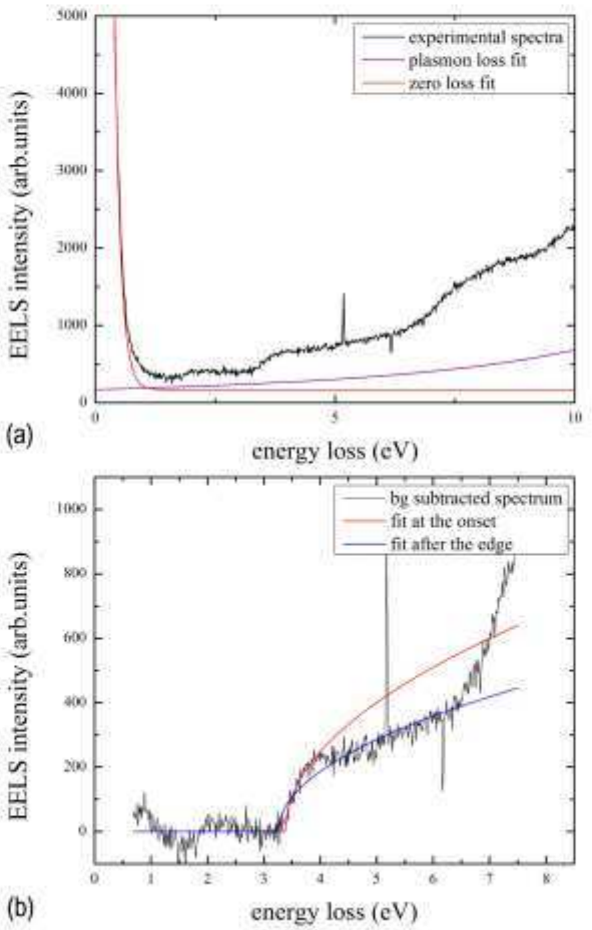

Fig. 8. Valence EELS of GaN from region E with (a) extrapolations of zero loss and plasmon loss peaks, (b) square-root fits to onset of spectrum intensity after zero loss and plasmon loss subtraction.

A monochromator with a slit in the energy-dispersive plane not only has the advantage of narrowing down the zero-loss peak but it also eliminates asymmetries due to the tails of the Fowler-Nordheim distribution for field emission and the Maxwell-Boltzmann distribution for heated filaments [32], and the intensity retained is proportional to the slit width and hence easily predictable [33]. When we attempt to fit the VEELS, the net intensity after background subtraction does not follow an ideal behaviour $\propto\sqrt{(E-E_g)}$, as would be expected from the density of states (DOS) for a bulk semiconductor with direct bandgap, E_g. The observed intensity increases steeper initially (close to linearly), then flattens before it again rises drastically. Fitting a square-root function near the DOS onset (red line in fig. 8(b); fit window 3.35-3.98 eV) gives a maximal R^2 =0.8933 and E_g=3.38eV, which is a reasonable value for GaN. Fitting after the DOS onset (blue line in fig. 8(b), fit window 2.85-6.41 eV) only gives R^2 =0.7861 and a lower apparent value of E_g=3.26eV. This shows some of the problems encountered when attempting to fit a square-root type DOS to high-quality EELS data: good fits do not necessarily produce the correct edge-onset, and if the fit windows are moved (or even constant offsets taken into account to model ZLP tails and/or a background possibly due to Cherenkov radiation) then the number of fitting parameters becomes large and several combinations can fit a spectrum reasonably well, however, which edge onset is most reliable is difficult to judge. This is a fundamental issue for determining bandgaps from VEELS, and for GaN, explored more fully in figure 9, the random-mean-square (rms) uncertainty in absolute bandgap determination remains of the order of ±0.1eV even for a monochromated instrument with an energy resolution far better than this (while fitting an analytical function over several channels could in theory produce sub-channel accuracy).

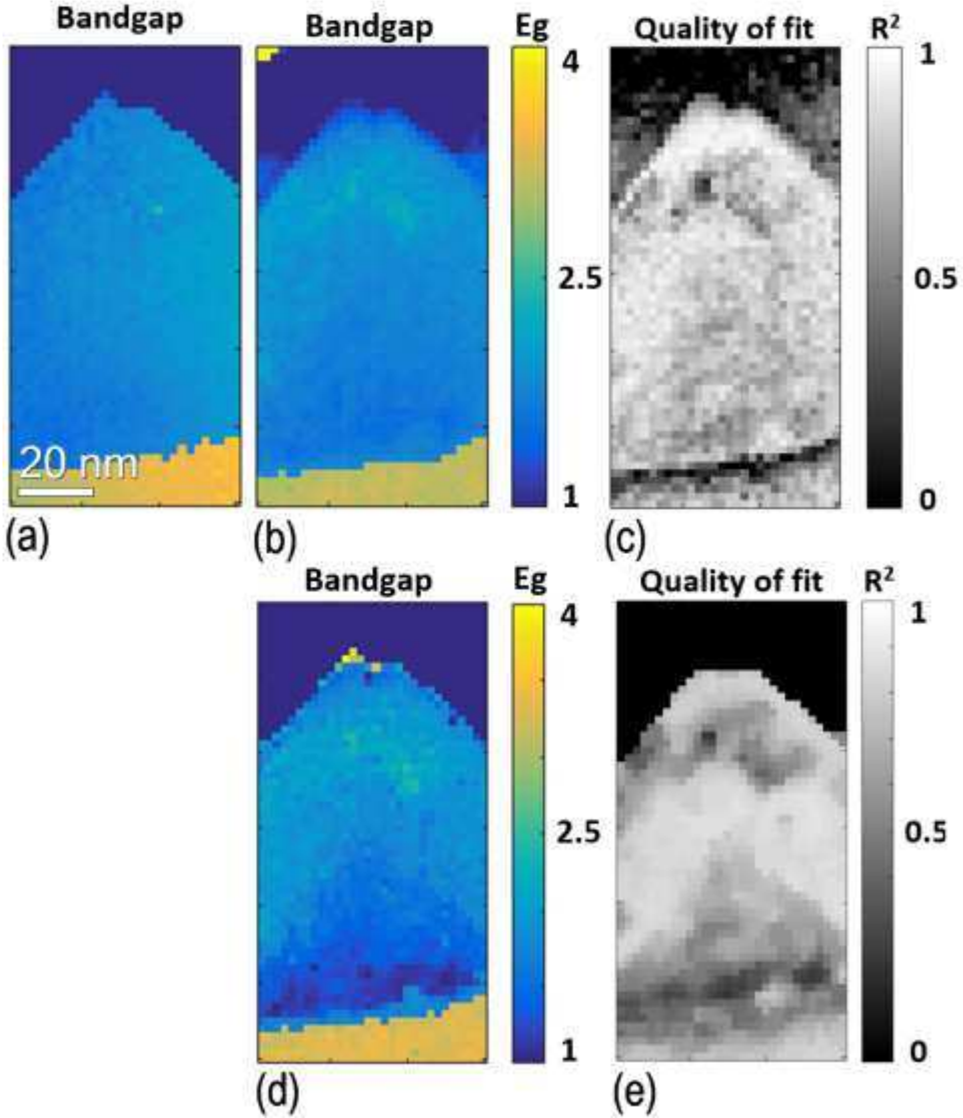

Fig. 9. Maps of (a, b, d) extracted direct bandgap E_g (in eV)and (c, e) R^2 for fits in (b, d), respectively, calculated for each point of spectrum image shown in figure 5. (a) has been calculated by extracting the VEELS from 0.7eV to 4 eV, smoothing it, fitting a spline function, differentiating it and finding the maximum in the first derivate map. This is quick and easy to process but provides no R^2 values as it is not a fit procedure. (b) has been calculated by subtracting a constant offset to account for zero loss and plasmon loss tails before fitting a function of form $300\times\sqrt{(E-E_g)}$ over a 1eV window in the range from 0.7eV to 5eV and maximizing R^2. (d) has been calculated by modeling and subtracting exponential tails for the ZLP and Lorentzian tails for the plasmon; the rest has been done as for (b).

The low-loss region directly after the zero loss peak (but overlapping with its tails) is due to interband transitions and thus reflects the density of states (DOS) near the conduction band. A simple differentiation after smoothing figure 9(a) and a calculation of the net signal by subtracting a constant offset to account for zero loss and plasmon loss tails (b), a rather common procedure, before fitting a square-root function of form $300\times\sqrt{(E-E_g)}$ over a 1eV window in the range from 0.7eV to 5eV and maximizing the R^2, yield qualitatively similar maps. Method (b) seems to work well in most areas except in the direct vicinity of the InGaN/GaN interface where the corresponding R^2 map in (c) decreases sharply. (d) has been calculated by subtracting exponential tails for the ZLP and Lorentzian tails for the plasmon; the rest has been done as for (b). This yields a slightly better curve fitting over-all and in particular near the InGaN/GaN interface region, but it yields comparably poor fits in the lower part of the InGaN. A complete numerical evaluation is included in Table II, demonstrating that even with superb energy resolution bandgap determination from VEELS is not as unambiguous as sometimes thought, and a precision better than the energy resolution of the spectrometer is probably not achievable due to ambiguities in removing zero loss peak and plasmon peaks. Our observation seems to be in good agreement with previous attempts of GaN bandgap measurements by VEELS, all of which reported error bars in the 0.1-0.2eV range [34-36] and, together with the additional problem of Cherenkov losses in most semiconductors [37], might explain why VEELS seems to generally work well for wide-bandgap materials [38] or semiconductors where the bandgap is known a-priori but can fail to correctly predict the bandgap of unknown semiconductor structures [39,40].

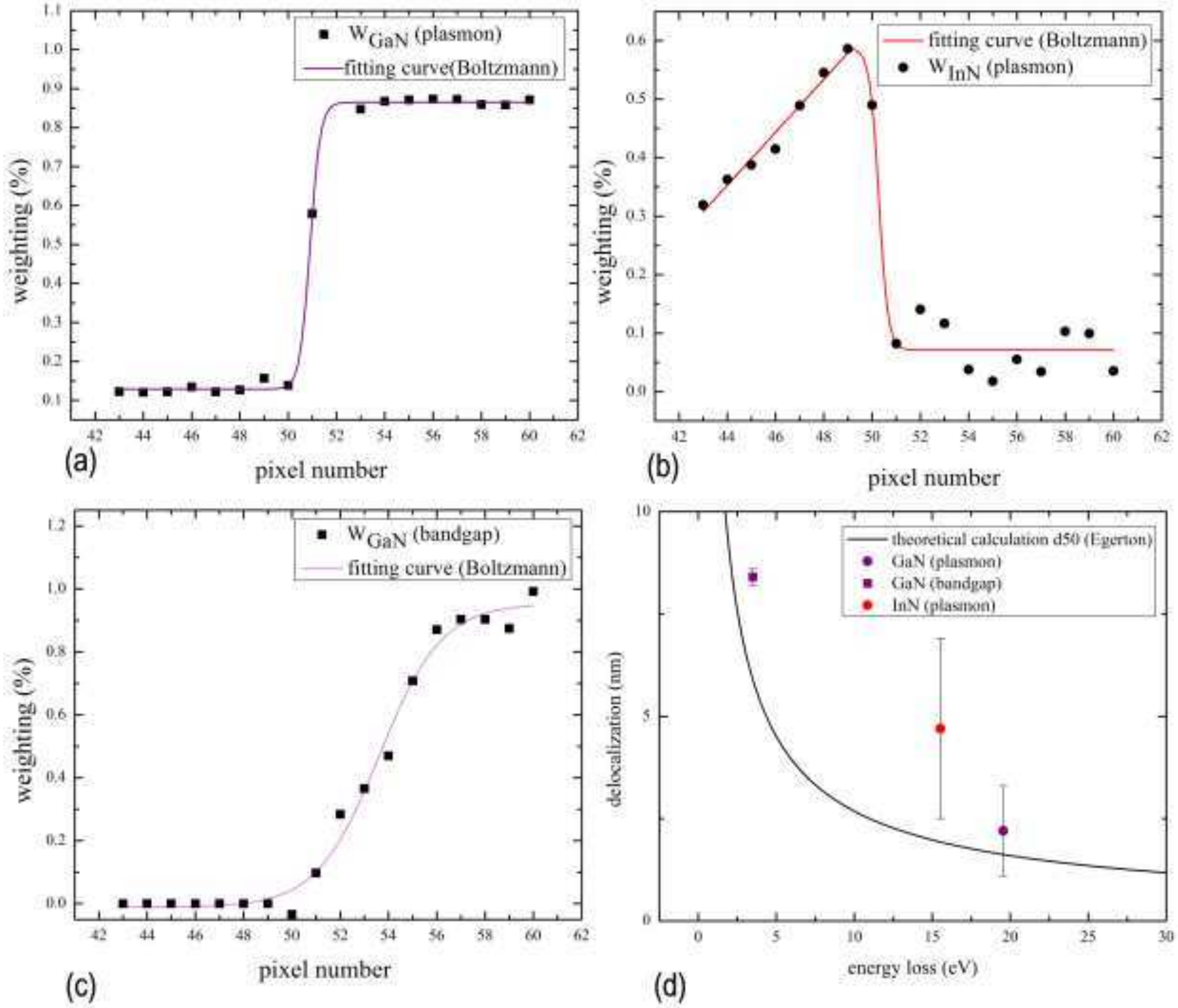

Fig. 10. Plots of the weight parameters from the least-squares fitting for (a) the GaN plasmon, (b) the InN plasmon and (c) the GaN band edge across the GaN/InGaN interface, as function of the pixel number in the growth direction. (d) compares the estimated 20% → 80% transition widths of the three signals with a simple model calculation for the delocalization of the inelastic scattering event due to finite momentum transfer [26].

It can be clearly seen from figure 10 that the plasmon transitions across the InGaN/GaN interface (the top row in the figure) are much sharper than the change in bandgap in figure 10(c) (bottom left), from the same spectrum image data, and the delocalization observed is in reasonable agreement with that expected from a simple model that evaluates the spatial resolution as the diameter d_{50} that contains 50% of the intensity from a Fourier transform of the finite energy and thus also finite momentum transfer based on mean scattering angles and finite collection aperture. This directly demonstrates plasmon losses may be regarded as local within the sampling limit of a few nanometres (here: 1-2 pixels, i.e. 2-4nm), while the bandgap is delocalized on a much wider scale. Physically, there would be no point in the definition of the bandgap for a crystal region smaller than that needed to hold a sufficiently large number of atoms forming the corresponding solid. What is worrying in Table II at the present is that for an indium content of x≥0.8 for region D we would expect a bandgap of the order of only ~1.0eV [41,22] while we actually measure 1.2-1.7eV. This may be tentatively explained by an apparent superposition of bandgaps from GaN and $In_{0.8}Ga_{0.2}N$ in EELS from the vicinity of the InGaN/GaN interface if the bandgaps of both materials (and in particular the lower bandgap) are noticeably delocalized, as figure 10 seems to imply. In fact, a close inspection of figure 8 reveals a weak kink in the EELS of GaN near ~1.5eV, which could be due to the persistence of information from the InGaN bandgap in the near-by GaN buffer: even though region E in the GaN is ~15nm from the InGaN/GaN interface, figure 10(d) indicates that the delocalisation increases inversely proportional to the bandgap energy; hence, information from GaN (E_g=3.4eV) leaks ~7nm into the InGaN, however, information from the InGaN (with E_g~1.7eV) leaks twice as wide into the GaN. This complicates the interpretation of bandgaps near interfaces enormously. Any algorithm fitting just one bandgap by a square-root function then would have to fail at an interface between two materials where both bandgaps overlap to differing degrees. The additional intensity ~0.5eV below the nominal bandgap reported in VEELS from an $In_{0.14}Ga_{0.86}N$ quantum well [30], on the other hand, cannot be attributed to a delocalisation effect because the bandgap from the surrounding GaN barrier would have been higher instead of lower than the bandgap of InGaN; it may be the result of a too large bandgap assumed for InN and a resulting offset in the relationship between composition and actual bandgap for InGaN alloys.

IV. CONCLUSIONS

Spectrum imaging of a cross-sectioned $In_{0.62}Ga_{0.38}N$ thin film specimen over the whole energy loss range allowed us to measure its chemical composition from different ionization losses and from plasmon peak shifts and to measure its electronic bandgap from the low-loss region. A direct correlation confirms that larger areas of increased indium content form underneath islands (with an indium content of x ≥0.9) and the bandgap decreases from ~2eV to 1.7eV, however, the bandgap change at the abrupt GaN/InGaN interface extends over more than 10nm. Sub-nanometre scale changes of the indium content observed elsewhere in the thin film by high-energy core loss spectroscopy are thus not expected to influence the bandgap directly, however, they may indirectly influence the optical properties by changing the local exciton binding energy and the stability of the excitons in the alloy [15].

The form of indium enrichment observed within a ~15nm high and ~60nm wide region under a facetted InGaN island differs from that previously observed within smaller InGaAs islands grown under the Stranski-Krastanow transition, which produces more rounded quantum dots: here, the indium enrichment commences directly at the InGaN/GaN interface and decreases towards the facetted surface, while InGaAs quantum dots have the highest indium content in their centres [42-44]. This suggests a slightly different process, presumable due to the wurtzite structure having a fundamentally different crystal symmetry from sphalerite, although compressive strain plays a role in both cases.

In terms of methodological development, it is interesting that the precision with which a direct bandgap can be determined is not governed by the energy resolution of the spectrometer but depends sensitively on the precise fitting procedure applied. Testing various alternative methods, we got a spread of typically ±0.1eV rms, however, this may not be sufficient for typical electronic applications where bandgaps would need to be known to much higher accuracy. The influence of doping could be detectable qualitatively if an undoped region were present in the same sample but doping effects will not be quantifiable at this level of accuracy. Interestingly, the simple approach of calculating a smoothed derivate and thresholding gave the best agreement for GaN of 3.41±0.07 eV, while the more widely used approach for determining direct bandgaps in semiconductors by fitting a square-root function to the VEELS is shown to depend sensitively on the choice of zero loss peak and plasmon modelling and subtraction (cf. figures 9(b) and (d)). In particular, we have shown that not only the intensity from the zero loss peak tail needs to be extrapolated and subtracted but also the tail from the plasmon.

ACKNOWLEDGMENT

We gratefully acknowledge the use of facilities within the LeRoy Eyring Center for Solid State Science at Arizona State University.

REFERENCES

1. P. Ruterana, G. Nouet, W. Van der Stricht, I Moerman and L. Considine: Chemical ordering in wurtzite $In_xGa_{1-x}N$ layers grown on (0001) sapphire by metalorganic vapor phase epitaxy. Appl. Phys. Lett. **72**(14), 1742 (1998).
2. D.M. Zhu, S. You, T. Detchprohm, T. Paskova, E.A. Preble, D. Hanser and C. Wetzel: Inclined dislocation-pair relaxation mechanism in homoepitaxial green GaInN/GaN light-emitting diodes. Phys. Rev B **81**(12), 125325 (2010).
3. Doppalapudi, S. N. Basu, K.F. Ludwig, Jr. and T.D. Moustakas: Phase separation and ordering in InGaN alloys grown by molecular beam epitaxy. J. Appl. Phys. **84**(3), 1389(1998).
4. Il-Kyu Park, M.K. Kwon, S.-H. Baek, Y.-W. Ok, T.-Y. Seong, S.-J. Park, Y.-S. Kim, Y.-T. Moon and D.-J. Kim: Enhancement of phase separation in the InGaN layer for self-assembled In-rich quantum dots. Appl. Phys. Lett. **87,** 061906 (2005).
5. Y.-S. Lin, K.-J. Ma, C. Hsu, S.-W. Feng, Y.-C. Cheng, C.-C. Liao, C.-C. Yang, C.-C. Chou, C.-M. Lee, and J.I. Chyi: Dependence of composition fluctuation on indium content in InGaN/GaN multiple quantum wells. Appl. Phys. Lett. **77**(19), 2988 (2000).
6. R. Singh, D. Doppalapudi, T.D. Moustakas and L.T. Romano: Phase separation in InGaN thick films and formation of InGaN/GaN double heterostructures in the entire alloy composition. Appl. Phys. Lett. **70**, 1089 (1997).
7. I.H. Ho and G.B. Stringfellow: Solid phase immiscibility in GaInN. Appl. Phys. Lett. **69**(18), 2701 (1996).
8. T. Matsuoka, T. Sasaki and A. Katsui: Growth and properties of a wide-gap semiconductor indium gallium nitride. Optoelectronics Dev. Technol. **5**(1), 53 (1990).
9. T. Matsuoka, N. Yoshimoto, T. Sasaki and A. Katsui: Wide-gap semiconductor InGaN and InGaAlN grown by MOVPE. J. Electron. Mater. **21**(2), 157 (1992).
10. S. Nakamura: Growth of $In_xGa_{1-x}N$ compound semiconductors and high-power InGaN/AlGaN double-heterostructure violet-light-emitting diodes. Microelectron. J. **25** (8), 651 (1994).
11. M. Shimizu, K. Hiramatsu and N. Sawaki: Metalorganic vapor-phase epitaxy growth of ($In_xGa_{1-x}N$/GaN) layered structures and reduction of indium droplets. J. Cryst. Growth. **145**, 209 (1994).

12. S. Nakamura, T. Mukai, M. Senoh, S. Nagahama and N. Iwasa: $In_xGa_{1-x}N$/ $In_yGa_{1-y}N$ superlattices grown on GaN films. J. Appl. Phys. **74**(6), 3911 (1993).
13. J.P. O'Neill, I.M. Ross, A.G. Cullis, T. Wang and P.J. Parbrook: Electron-beam-induced segregation in InGaN/GaN multiple-quantum wells. Appl. Phys. Lett. **83**(10), 1965 (2003).
14. T.M. Smeeton, M.J. Kappers, J.S. Barnard, M.E. Vickers and C.J. Humphreys: Electron-beam-induced strain within InGaN quantum wells: false indium "cluster" detection in the transmission electron microscope. Appl. Phys. Lett. **83**(26), 5419 (2003).
15. C.J. Humphreys: Does In form In-rich clusters in InGaN quantum wells? Philos. Mag. **87**(13), 1971 (2007).
16. K.H. Baloch, A.C. Johnston-Peck, K. Kisslinger, E.A. Stach and S. Gradecak: Revisiting the "In-clustering" question in InGaN through the use of aberration corrected electron microscopy below the knock-on threshold. Appl. Phys. Lett. **102**, 191910 (2013).
17. X. Wang, M.-P. Chauvat, P. Ruterana and T. Walther: Investigation of phase separation in InGaN alloys by plasmon loss spectroscopy in a TEM. MRS Advances (2016) published online 5 August 2016 with DOI: 10.1557/adv2016.542
18. X. Wang, M.P. Chauvat, P. Ruterana and T. Walther: Combination of electron energy-loss spectroscopy and energy-dispersive X-ray spectroscopy to determine indium concentration in InGaN thin film structures. Semicond. Sci. Technol. **30**(11), 114011 (2015).
19. T. Walther, F. Wolf, A. Recnik and W. Mader: Quantitative microstructural and spectroscopic investigation of inversion domain boundaries in zinc oxide ceramics sintered with iron oxide. Int. J. Mater. Res. **97**, 934 (2006).
20. O.L. Krivanek, J.P Ursin, N.J. Bacon, G.J. Corbin, N. Dellby, P. Hrncirik, M.F. Murfitt, C.S. Own and Z.S. Szylagyi: High-energy-resolution monochromator for aberration-corrected scanning transmission electron microscope / electron energy-loss spectroscopy. Phil. Trans. Roy. Soc. Lond. A **367** (1903) 3683 (2009).
21. T.P. Bartel, P. Specht, J.C. Ho and C. Kisielowski: Phase separation in $In_xGa_{1-x}N$, Philos. Mag. **87**(13), 1983 (2007).
22. G. Orsal, Y. El Gmili, N. Fressengeas, J. Streque, R. Djerboub, T. Moudakir, D. Sundaram, A. Ougazzaden and J.P. Salvestrini: Bandgap energy bowing parameter of strained and relaxed InGaN layers. Opt. Mater. Express **4**(5), 1030 (2014).
23. T. Walther: An improved approach to quantitative X-ray microanalysis in (S)TEM: thickness dependent k-factors. Proc EMAG 2009, Sheffield. J. Phys. Conf. Ser. **241**, 012016 (2010).
24. T. Walther and X. Wang: Self-consistent method for quantifying indium content from X-ray spectra of thick compound semiconductor specimens in a transmission electron microscope J. Microsc. **252** :2, 151 (2016).
25. H. Amari, I.M. Ross, T. Wang and T. Walther: Characterization of InGaN/GaN epitaxial layers by aberration corrected TEM/STEM. Phys. Stat. Sol. C **9** (3-4), 546 (2012).
26. R.F. Egerton: Electron Energy-Loss Spectroscopy in the Electron Microscope, Plenum Press, New York, 2nd ed. (1996).
27. V.C. Angadi, C. Abhayaratne and T. Walther: Automated background subtraction technique for electron energy-loss spectroscopy and application to semiconductor heterostructures. J. Microsc. **262**(2), 157 (2016).
28. P.J. Thomas and R.D. Twesten: A simple, model based approach for robust quantification of EELS spectra and spectrum-images. Microsc. Microanal. **18** (suppl. 2), 968 (2012).

29. J. Scott, P.J. Thomas, M. MacKenzie, S. McFadzean, J. Wilbrink, A.J. Craven and W.A.P. Nicholson: Near-simultaneous dual energy range EELS spectrum imaging. Ultramicrosocpy **108**(12), 1586 (2008).
30. J.R. Jinschek, R. Erni, N.F. Gardner, A.Y. Kim and C. Kisielowski: Local indium segregation and band gap variations in high efficiency green light emitting InGaN/GaN diodes. Solid State Comm. **137**, 230 (2006).
31. M. Albrecht, V. Grillo, J. Borysiuk, T. Remmele. H.P. Strunk, T. Walther, W. Mader, P. Prystawko, M. Leszczynski, I. Grzegory and S. Porowski: Correlating compositional, structural and optical properties of InGaN quantum wells by transmission electron microscopy. Proc. Microsc. Semicond. Mater. Conf. 2001, Oxford. Inst. Phys. Conf. Ser. **169**, 267 (2001).
32. R. Erni and N.D. Browning: Valence electron energy-loss spectroscopy in monochromated scanning transmission electron microscopy. Ultramicroscopy **104** (3-4), 176 (2005).
33. T. Walther and H. Stegmann: Preliminary results from the first monochromated and aberration corrected 200-kV field-emission scanning transmission electron microscope. Microsc. & Microanal. **12**(6), 498 (2006).
34. G. Brockt and H. Lakner: Nanoscale EELS analysis of dielectric function and bandgap properties in GaN and related materials. Micron **31**, 435 (2000).
35. S. Schamm and G. Zanchi: Study of the dielectric properties near the band gap by VEELS: gap measurement in bulk materials. Ultramicroscopy **96**, 559 (2003).
36. J.M. Manual, C.T. Koch, V.B. Özdöl, W. Sigle, P.A. van Aken, R. Garcia and F.M. Morales: Inline electron holography and VEELS for the measurement of strain in ternary and quaternary (In,Al,Ga)N alloyed thin films and its effect on bandgap energy. J. Microsc. **261**(1), 27 (2016).
37. Stöger-Pollach and P. Schattschneider: The influence of relativistic energy losses on bandgap determination using valence EELS. Ultramicroscopy **107**(12), 1178 (2007).
38. H. Müllejans and R.H. French: Insights into the electronic structure of ceramics through quantitative analysis of valence energy-loss spectroscopy. Microsc. Microanal. **6**(4), 297 (2000).
39. P. Specht, J.C. Ho, X. Xu, R. Armitage, E.R. Weber, R. Erni and C. Kisielowski: Band transitions in wurtzite GaN and InN determined by valence electron energy loss spectroscopy. Sol. State Comm. **135**, 340 (2005).
40. R. Erni and N.D. Browning: Quantification of the size-dependent energy gap of individual CdSe quantum dots by valence electron energy-loss spectroscopy. Ultramicroscopy **107**(2-3), 267 (2007).
41. R.R. Pelá, C. Caetano, M. Marques, L.G. Ferreira, J. Furthmüller and L.K. Teles: Accurate band gaps of AlGaN, InGaN and AlInN alloys calculations based on LDA-1/2 approach. J. Appl. Phys. **98**(15), 151907 (2011).
42. T. Walther, A.G. Cullis, D.J. Norris and M. Hopkinson: Nature of the Stranski-Krastanow transition during epitaxy of InGaAs on GaAs. Phys. Rev. Lett. **86** (11), 2381 (2001)
43. T. Walther, A.G. Cullis, D.J. Norris and M. Hopkinson: How InGaAs islands form on GaAs substrates: the missing link in the explanation of the Stranski-Krastanow transition. Proc. Microsc. Semicond. Mater. Conf. 2001, Oxford. Inst. Phys. Conf. Ser. **169**, 85 (2001).
44. A.G. Cullis, D.J. Norris, T. Walther, M.A. Migliorato and M. Hopkinson: Stranski-Krastanow transition and epitaxial island growth. Phys. Rev. B 66, 081305R (2002).